



Universiteit
Leiden
The Netherlands

ALMA measures molecular gas reservoirs comparable to field galaxies in a low-mass galaxy cluster at $z = 1.3$

Williams, C.C.; Alberts, S.; Spilker, J.S.; Noble, A.G.; Stefanon, M.; Willmer, C.N.A.; ... ; Whitaker, K.E.

Citation

Williams, C. C., Alberts, S., Spilker, J. S., Noble, A. G., Stefanon, M., Willmer, C. N. A., ... Whitaker, K. E. (2022). ALMA measures molecular gas reservoirs comparable to field galaxies in a low-mass galaxy cluster at $z = 1.3$. *The Astrophysical Journal*, 929(1).
doi:10.3847/1538-4357/ac58fa

Version: Publisher's Version
License: [Creative Commons CC BY 4.0 license](#)
Downloaded from: <https://hdl.handle.net/1887/3561988>

Note: To cite this publication please use the final published version (if applicable).



ALMA Measures Molecular Gas Reservoirs Comparable to Field Galaxies in a Low-mass Galaxy Cluster at $z = 1.3$

Christina C. Williams¹ , Stacey Alberts¹ , Justin S. Spilker^{2,3,10} , Allison G. Noble⁴ , Mauro Stefanon⁵ , Christopher N. A. Willmer¹ , Rachel Bezanson⁶ , Desika Narayanan^{7,8} , and Katherine E. Whitaker^{8,9}

¹ Steward Observatory, University of Arizona, 933 North Cherry Avenue, Tucson, AZ 85721, USA

² Department of Astronomy, University of Texas at Austin, 2515 Speedway, Stop C1400, Austin, TX 78712, USA

³ Department of Physics and Astronomy and George P. and Cynthia Woods Mitchell Institute for Fundamental Physics and Astronomy, Texas A&M University, 4242 TAMU, College Station, TX 77843-4242, USA

⁴ School of Earth and Space Exploration, Arizona State University, Tempe, AZ 85287-1404, USA

⁵ Leiden Observatory, Leiden University, NL-2300 RA Leiden, The Netherlands

⁶ Department of Physics and Astronomy and PITT PACC, University of Pittsburgh, Pittsburgh, PA 15260, USA

⁷ Department of Astronomy, University of Florida, 211 Bryant Space Science Center, Gainesville, FL 32611, USA

⁸ Cosmic Dawn Center (DAWN), Denmark

⁹ Department of Astronomy, University of Massachusetts, Amherst, 710 N. Pleasant Street, Amherst, MA 01003, USA

Received 2021 December 15; revised 2022 February 23; accepted 2022 February 24; published 2022 April 11

Abstract

We report the serendipitous discovery of an overdensity of CO emitters in an X-ray-identified cluster ($\text{Log}_{10} M_{\text{halo}}/M_{\odot} \sim 13.6$ at $z = 1.3188$) using ALMA. We present spectroscopic confirmation of six new cluster members exhibiting CO(2–1) emission, adding to two existing optical/IR spectroscopic members undetected in CO. This is the lowest-mass cluster to date at $z > 1$ with molecular gas measurements, bridging the observational gap between galaxies in the more extreme, well-studied clusters ($\text{Log}_{10} M_{\text{halo}}/M_{\odot} \gtrsim 14$) and those in group or field environments at cosmic noon. The CO sources are concentrated on the sky (within ~ 1 arcmin diameter) and phase space analysis indicates the gas resides in galaxies already within the cluster environment. We find that CO sources sit in similar phase space as CO-rich galaxies in more massive clusters at similar redshifts (have similar accretion histories) while maintaining field-like molecular gas reservoirs, compared to scaling relations. This work presents the deepest CO survey to date in a galaxy cluster at $z > 1$, uncovering gas reservoirs down to $M_{\text{H}_2} > 1.6 \times 10^{10} M_{\odot}$ (5σ at 50% primary beam). Our deep limits rule out the presence of gas content in excess of the field scaling relations; however, combined with literature CO detections, cluster gas fractions in general appear systematically high, on the upper envelope or above the field. This study is the first demonstration that low-mass clusters at $z \sim 1-2$ can host overdensities of CO emitters with surviving gas reservoirs, in line with the prediction that quenching is delayed after first infall while galaxies consume the gas bound to the disk.

Unified Astronomy Thesaurus concepts: [High-redshift galaxy clusters \(2007\)](#); [Molecular gas \(1073\)](#); [Galaxy evolution \(594\)](#)

1. Introduction

One of the most transformational events in the lives of galaxies is the cessation of active star formation (quenching), marking a transition to passive evolution. Environment is a strong regulator of star formation activity, operating independently of mass-dependent quenching to $z < 1$, and producing largely quenched populations in the low-redshift universe (Dressler 1980; Balogh et al. 1998; Lewis et al. 2002; Peng et al. 2010).

By the present day ($z = 0$) the era of active growth of galaxies in clusters through star formation is mostly complete. Moreover, at $z \lesssim 1$, clusters are already largely quiescent in their cores (e.g., Patel et al. 2009; Finn et al. 2010; Vulcani et al. 2010; Muzzin et al. 2012). However, at $z = 1-2$, the discovery of significant populations of star-forming galaxies in clusters (i.e., Cooper et al. 2006; Hilton et al. 2010; Tran et al. 2010; Fassbender et al. 2011; Hayashi et al. 2011; Tadaki et al. 2011; Brodwin et al. 2013;

Zeimann et al. 2013; Alberts et al. 2014, 2016, 2021; Bayliss et al. 2014; Fassbender et al. 2014; Santos et al. 2014, 2015; Ma et al. 2015; Alberts et al. 2016, 2021) indicates a reversal in the star formation rate (SFR)–density relation at higher redshifts, albeit with significant cluster-to-cluster variation (i.e., Alberts et al. 2016). Massive clusters at this transition epoch from $z = 1-2$ have been shown to host field-like (obscured) star formation (Brodwin et al. 2013; Alberts et al. 2014, 2016, 2021), alongside a significant ramp-up of the environmental quenching efficiency (Nantais et al. 2017). Understanding this epoch is pivotal to our understanding of environment over cosmic time, linking the proto-cluster regime to local clusters through a critical era of galaxy buildup.

Finally, at $z > 2$, the majority of significant overdensities are expected to be proto-clusters: an early phase where structures are not yet virialized and are still collapsing, and subtend a large area on the sky (Chiang et al. 2013, 2017; Casey 2016) prior to establishing a hot intra-cluster medium (ICM). Proto-clusters are typically signposted by their dominant population of star-forming galaxies (traced by Ly α , H α , or dust continuum emission). Proto-clusters likely contribute a significant portion of the cosmic SFR density while in this active phase of growth via star formation (Chiang et al. 2017), prior to the era of increased quenching efficiency at $z = 1-2$. We note that

¹⁰ NHFP Hubble Fellow.

establishing the presence of an ICM at high redshift can be challenging. Cases exist where X-ray emission does not originate from the ICM, as has been seen in some high-redshift proto-clusters (Wang et al. 2016; Champagne et al. 2021). Direct detection via X-rays further suffers from surface bright dimming. Sunayev–Zeldovich surveys, while in principle redshift independent, may not be sensitive to ICMs with low temperatures or may be effected by upscattering of cosmic microwave background photons from the brightest cluster galaxy (BCG; e.g., Chatterjee et al. 2010; Hall et al. 2019).

Quenching processes likely initiate during infall into the dense cluster environment. A critical constraint on the impact of environment is the cold molecular gas content in galaxies, the fuel for star formation. Unfortunately, the number of true virialized galaxy cluster candidates (confirmed by a hot ICM, or inferred from a red sequence) at this critical era of $1 < z < 2$ that also have molecular gas constraints is small (Hayashi et al. 2017; Noble et al. 2017; Rudnick et al. 2017; Stach et al. 2017; Coogan et al. 2018; Tadaki et al. 2019). This is a severe limitation given that current studies indicate significant cluster-to-cluster variation in star formation activity (Geach et al. 2006; Alberts et al. 2016). Targeted CO observations in clusters tend to be conservative, choosing to observe rich overdensities to maximize success rate. The known CO emitters in these high-mass clusters ($\text{Log}_{10}M_{\text{halo}}/M_{\odot} \gtrsim 14$) to date exhibit field-like or enhanced molecular gas content (i.e., Noble et al. 2017; Rudnick et al. 2017; Hayashi et al. 2018). While based on a small sample, these results suggest that enhanced gas fractions could be prevalent in high-density environments at high redshift. However, due to the challenging nature of high-redshift CO observations, these surveys have relatively high molecular gas detection limits, which can cause a biased picture by detecting only the most gas-rich sources. Blind and deep CO spectroscopy would provide a less biased and more comprehensive picture of gas content in cluster galaxies, but unfortunately is very expensive to obtain.

Fortunately, we recently conducted an ultra-deep Atacama Large Millimeter/submillimeter Array (ALMA) spectroscopic campaign targeting CO(2–1) emission in massive quiescent galaxies at $z \sim 1.5$ (Williams et al. 2021). Our data serendipitously discovered that one target resides in a previously unknown overdensity of CO emitters. The structure is an X-ray-identified galaxy cluster with a halo mass of $\text{Log}_{10}M_{\text{halo}}/M_{\odot} = 13.6$ (Gozaliasl et al. 2019) which, until our ALMA discovery, lacked spectroscopic confirmation. We have identified six cluster members based on their CO(2–1) emission within 225 kpc of the central quiescent galaxy. This low-mass cluster presents a rare addition to the current CO-observed samples, expanding the halo mass range covered at $z > 1$, and thus represents an opportunity to study previously unexplored parameter space in cluster evolution.

In Section 2 we present the multiwavelength evidence for the galaxy cluster hosting our galaxies, our ALMA data, and galaxy sample properties. In Sections 3 and 4 we present the cold molecular gas reservoir measurements and discuss our results in the context of both gas reservoirs measured in field galaxies, as well as other (typically more massive) clusters, offering a unique opportunity to bridge the observational gap between these vastly different galaxy environments at $z > 1$. Throughout this work we assume a Λ CDM cosmology with $H_0 = 70 \text{ km s}^{-1} \text{ Mpc}^{-1}$, $\Omega_M = 0.3$, $\Omega_{\Lambda} = 0.7$, and a Kroupa (2001) initial mass function.

2. Data

2.1. Evidence for the Galaxy Cluster

This overdensity was first identified photometrically in COSMOS imaging using Voronoi Tessellation (Scoville et al. 2013), which demonstrated a significant and concentrated surface overdensity of more than five galaxies per comoving Mpc^2 between $1.28 < z < 1.34$. A later analysis of deep XMM and Chandra X-ray data revealed extended emission indicating the presence of an ICM, with a well defined X-ray center (Gozaliasl et al. 2018, 2019). The X-ray center is very close to a massive $\text{Log}_{10}M^*/M_{\odot} = 11.2$ quiescent galaxy targeted with ALMA spectroscopy (hereafter referred to as source 0) in Williams et al. (2021) at $z = 1.322$. The group catalog published by Gozaliasl et al. (2019) identified this overdensity (ID = 377) as a cluster with $\text{Log}_{10}M_{\text{halo}}/M_{\odot} = 13.6 \pm 0.1$ (M_{200} measured based on X-ray luminosity), an estimated velocity dispersion of 360 km s^{-1} , and a virial radius of $R_{200} \sim 50''$ ($\sim 0.4 \text{ Mpc}$). Gozaliasl et al. (2019) identified candidate cluster members from the COSMOS2015 photometric catalog (Laigle et al. 2016). A cluster redshift of $z = 1.319$ was assigned based on the sole spectroscopic redshift among candidate cluster members (Hasinger et al. 2018, referred to herein as source 7). Gozaliasl et al. (2019) label structures with $\text{Log}_{10}M_{\text{halo}}/M_{\odot} < 14$ as low-mass clusters or groups. Given that the boundary between massive groups and low-mass clusters is generally ill defined in the literature, in this work we consider this structure to be a low-mass cluster, due to its extended X-ray emission and likelihood of hosting a massive BCG; see sources 0 and 7 described below.

We note that, given the modest significance (3.3σ ; Gozaliasl et al. 2019) of the X-ray detection, hydrostatic equilibrium (i.e., virialization) was assumed in order to determine a halo mass from the X-ray emission using the low-scatter scaling relations for relaxed clusters (e.g., Kravtsov et al. 2006; Vikhlinin et al. 2009; Leauthaud et al. 2010; Mantz et al. 2010). Significant deviations from hydrostatic equilibrium in clusters with an established ICM can result from merger events (Randall et al. 2002; Poole et al. 2007; Wik et al. 2008). The ICM temperature reported in Gozaliasl et al. (2019) is $1.34 \pm 0.16 \text{ keV}$, a relatively low temperature favoring the assumption that the cluster is virialized and disfavoring a non-relaxed or merging system. However, given the temperature estimate is derived directly from L_x using the L_x – T relation (e.g., Markevitch 1998) any deviations from hydrostatic equilibrium cannot be distinguished in the existing data. Therefore we also assume a virialized state applies for both the ICM gas and cluster members (see Rosati et al. 2002 for a review) throughout this work.

The location of the X-ray center, Voronoi-identified overdensity, candidate cluster members, and our new spectroscopically confirmed galaxies (introduced in the next sections) are shown in Figure 1.

2.2. ALMA Data

The ALMA observations probing the CO overdensity were carried out in project 2018.1.01739.S (PI: Williams) for target galaxy 34879 (Williams et al. 2021, listed as source ID = 0 in Table 1). The field was observed on 2018 December 18 and 2019 January 17 using the Band 3 (3 mm) receivers. The correlator was configured to center the CO(2–1) line for 34879

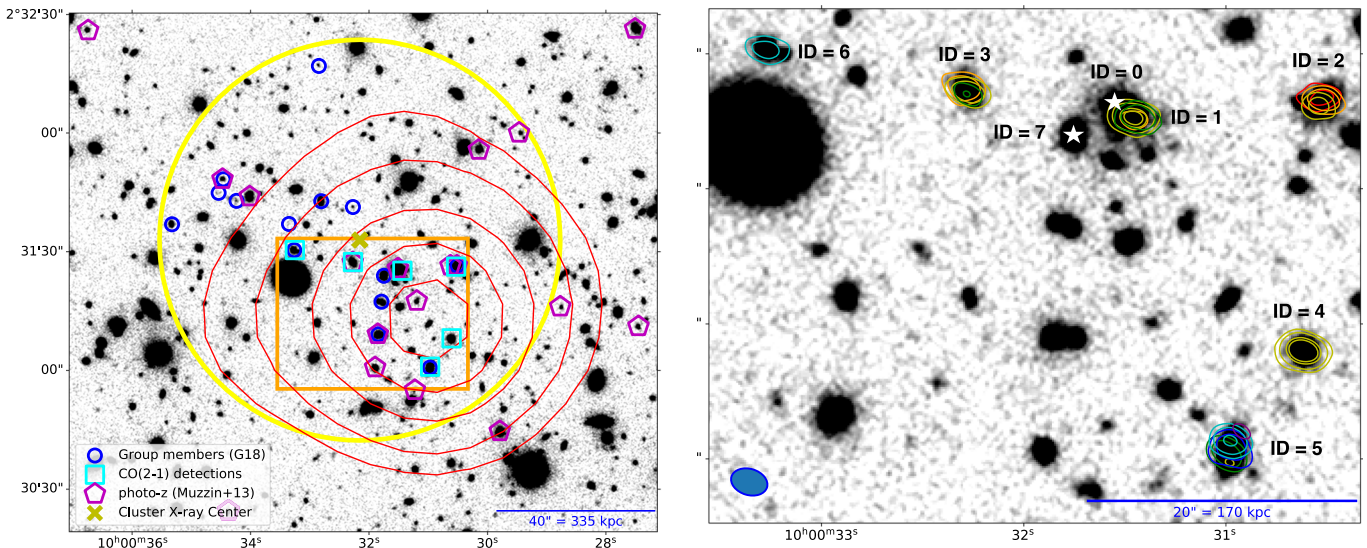


Figure 1. UltraVISTA K-band image of the cluster field (grayscale) identifying cluster members. Left: large-scale image of the galaxy cluster with Voronoi galaxy overdensity per comoving Mpc^{-2} , in a redshift slice $1.28 < z < 1.34$ based on photometric redshift (red contours; Scoville et al. 2013). Galaxy group members (Gozaliasl et al. 2019) are in blue and other galaxies with similar photometric redshift of $1.28 < z < 1.35$ in magenta. New CO(2–1) detections from this work are shown in green. The X-ray cluster center is indicated by a small yellow circle with R_{200} as a larger yellow circle. Right: zoom-in on the region of the cluster with CO emitters. Contours indicate the CO(2–1) emission measured with ALMA (colors represent different 200 km s^{-1} velocity channels as in Figure 2). Two spectroscopic members with no CO(2–1) emission are identified with white stars. The ALMA synthesized beam is shown by the blue shaded ellipse ($2''.7 \times 1''.9$).

at $z = 1.322$ (99.284 GHz) within a spectral window of 1.875 GHz width, providing $\sim 5500 \text{ km s}^{-1}$ of bandwidth centered on the expected frequency of the CO line. Three additional spectral windows were used for continuum observations. The target was observed for a total of ~ 3.2 hr on-source. The array was in a compact configuration yielding a synthesized beam size of $2''.7 \times 1''.9$. Our data reduction procedure is outlined in Williams et al. (2019, 2021). The spectral cube of our reduced data has a resulting noise of $\approx 30 \mu\text{Jy beam}^{-1}$ in a 400 km s^{-1} channel measured near the rest-frequency of the CO(2–1) line ($\nu_{\text{rest}} = 230.538 \text{ GHz}$). The 100 GHz continuum data reach a sensitivity $\approx 5 \mu\text{Jy beam}^{-1}$ at the phase center. None of our newly discovered CO-emitters are significantly detected in the continuum, though source IDs 1 and 5 are marginally detected at the $2 \lesssim \sigma \lesssim 3$ level. These non-detections are unsurprising given the depth of our data and typical assumptions for the dust temperature, emissivity, and gas-to-dust mass ratio.

We significantly detected six sources of CO(2–1) line emission (at $>5\sigma$, referenced herein as source IDs 1–6), easily identified through inspection of the CO spectral cube. To extract spectra for each source, we used the `uvmultifit` package (Martí-Vidal et al. 2014) to fit multiple pointlike sources to the visibility data. Briefly, we perform a joint fit of all sources at each frequency channel, using approximate by-eye source positions as the starting estimates, with the exception of the spectroscopically identified but CO-undetected source ID 0, whose position is fixed to the phase center.

To measure CO(2–1) line fluxes and luminosities, we first fit a simple Gaussian profile to the extracted spectrum. In a few cases (ALMA ID = 2, 3, and 5) there is clear evidence for either gas rotation or multiple components in the CO(2–1) spectrum; we note that the morphologies of these galaxies in the high-resolution Hubble Space Telescope (HST)/Advanced Camera for Surveys (ACS) imaging are consistent with only a single galaxy within the ALMA beam. For these sources, we also fit a double Gaussian model, where we fix the FWHM to

be the same for both components, and define the redshift as the mean of the two peaks. Our results are not dependent on the single or double Gaussian assumption. We adopt the double Gaussian to model the line for those three sources. To measure the integrated CO(2–1) line flux, we integrate the observed spectrum over the frequency range where the Gaussian model is greater than 5% of the peak value and add in quadrature each channel rms to measure the integrated line flux uncertainty. Integrating the Gaussian model produces consistent integrated line flux measurements within the uncertainties, but our method more accurately captures the line flux in cases where the line profile is not perfectly described as a Gaussian.

Two existing optical spectroscopically confirmed galaxies (undetected in CO) are associated with this overdensity: the galaxy associated with the group by Gozaliasl et al. (2019) measured by Hasinger et al. (2018, source 7) and our target quiescent galaxy (source 0; Belli et al. 2014; Williams et al. 2021), in addition to our six new CO(2–1) sources. Our measurement of upper limits for the two undetected galaxies and our procedure to convert from CO(2–1) line luminosity to M_{H_2} follow those outlined in Williams et al. (2021). Briefly, we use a channel width of 500 km s^{-1} to measure upper limits to M_{H_2} for the two undetected sources with spectroscopic redshifts (IDs 0 and 7).

To convert CO(2–1) luminosity to a molecular gas mass, M_{H_2} , we assume a luminosity ratio between the CO(2–1) and CO(1–0) transitions $r_{21} = 0.8$ in temperature units and a CO– H_2 conversion factor $\alpha_{\text{CO}} = 4.4 \text{ (K km s}^{-1} \text{ pc}^2)^{-1}$. Based on fundamental metallicity relations (e.g., Genzel et al. 2015; Tacconi et al. 2018), our galaxies (with exception of ID = 1) likely have high metallicity, close to solar ($\text{Log}_{10} Z/Z_{\odot} \sim 0.1$). Models for the variation of α_{CO} at these high metallicities do not predict much variation and are consistent with a Milky Way-like conversion (see, e.g., Figure 9 in Bolatto et al. 2013 and references therein). This indicates that it is unlikely that α_{CO} could be higher, and therefore the Milky Way-like value is a reasonable, and even conservative assumption for our sample.

Table 1
Optical to Radio Spectral Energy Distribution Properties

ALMA ID	UltraVISTA ID	R.A.	Decl.	$\text{Log}_{10}M^*$	SFR_{SED}	$\text{SFR}_{\text{UV+IR}}$	$\text{SFR}_{\text{radio}}$	SFR_{best}
0	210589 ^a	150.131380	2.523800	11.22	1.47	22.90	<57.23 ^c	1.47
1	–99	150.131012	2.523659	9.59	45.43	–99.00	<69.25 ^d	69.25 ^d
2	210543	150.127225	2.523947	11.04	9.10	1.28	29.50	29.50
3	210530	150.134492	2.524271	10.58	33.13	22.14	25.04	25.04
4	210038	150.127542	2.518901	10.62	29.17	32.77	24.99	24.99
5	209948	150.129054	2.516903	11.09	92.37	56.59	37.06	37.06
6	210534	150.138625	2.525131	10.32	18.43	0.68	–99.00	18.43
7 ^b	210442	150.132310	2.523304	10.59	4.79	207.76	87.26	87.26

Notes.

^a Referred to with ID = 34879 in Belli et al. (2014) and Williams et al. (2021).

^b Spectroscopically confirmed member from Hasinger et al. (2018).

^c Should be considered an upper limit, since likely the radio flux is dominated by an active galactic nucleus as described in Section 2.4.

^d Should be considered an upper limit, because it is blended with source 0 in the IR as described in Section 2.4.

Table 2
Molecular Gas Properties

ALMA ID	z_{co}	FWHM (km s^{-1})	$v_{\text{offset}}^{\text{b}}$ (km s^{-1})	$S_{\nu} dv^{\text{c}}$ (mJy km s^{-1})	$L'_{\text{co}}^{\text{c}}$ ($10^9 \text{ K km s}^{-1} \text{ pc}^2$)	$M_{\text{H}_2}^{\text{c}}$ ($10^{10} M_{\odot}$)
0 ^a	1.322	...	414	<13.8	<0.33	<0.55
1	1.3174	332 ± 30	–177	283.1 ± 21.1	6.5 ± 0.5	3.6 ± 0.3
2	1.3164	554 ± 56	–312	295.1 ± 20.4	6.7 ± 0.5	3.7 ± 0.3
3	1.3170	411 ± 42	–229	242.9 ± 15.2	5.5 ± 0.3	3.1 ± 0.2
4	1.3171	129 ± 8	–214	279.3 ± 14.2	6.4 ± 0.3	3.5 ± 0.2
5	1.3202	545 ± 49	179	472.5 ± 30.4	10.8 ± 0.7	6.0 ± 0.4
6	1.3220	206 ± 35	413	159.6 ± 20.9	3.7 ± 0.5	2.0 ± 0.3
7 ^a	1.319	...	24	<13.9	<0.33	<0.55

Notes.

^a Undetected in ALMA data but with spectroscopic coverage of CO(2–1), limiting flux measured in a 500 km s^{-1} channel. We provide 1σ upper limits for L'_{co} and 3σ upper limits for M_{H_2} assuming $R_{21} = 0.8$ in temperature units, $\alpha_{\text{co}} = 4.4$. Molecular gas masses can be rescaled under different assumptions as $M_{\text{H}_2} \times (0.8/21)(\alpha_{\text{co}}/4.4)$.

^b Velocity offset relative to the cluster redshift ($z = 3.188$) we calculate in Section 2.5.

^c Integrating observed spectrum and propagating channel errors.

Additionally, the presence of warm or high-velocity dispersion gas would only serve to reduce α_{co} , and therefore the inferred gas masses, even further (Narayanan et al. 2012). We note that our ID = 1 source is above the main sequence (Figure 3), a characteristic of starburst galaxies is that they may have lower $\alpha_{\text{CO}} \sim 1$ (e.g., Bolatto et al. 2013). This would serve to lower the inferred M_{H_2} from the CO(2–1) line. However, we find that lowering α_{CO} for this galaxy does not change our conclusions in the following sections, and therefore present all results assuming the same $\alpha_{\text{co}} = 4.4 \text{ (K km s}^{-1} \text{ pc}^2)^{-1}$. Our molecular gas properties and limits are listed in Table 2 and their CO spectra and images are presented in Figure 2.

2.3. Optical/IR Data

We have a total of eight spectroscopic cluster members, including the two galaxies with optical spectra previously measured (IDs 0, 7) and our six new CO(2–1) sources (IDs 1–6). This cluster lies in the gap between WFC3 and ACS grism data from the 3DHST program and therefore no grism redshifts are available.

We identified counterparts to galaxies with CO(2–1) emission using the ULTRAVISTA photometry catalog (Muzzin et al. 2013a). Five out of six CO sources have counterparts, with the exception of the source with ALMA ID = 1. This source was previously noted in Williams et al. (2021) to be a companion of

the target quiescent galaxy (ID = 0) at a distance of $\sim 1''$ and velocity offset of 600 km s^{-1} . This velocity offset is significantly larger than the expected spectroscopic redshift uncertainty, given that the measured velocity dispersion of the quiescent galaxy $\sigma = 213 \pm 53 \text{ km s}^{-1}$ (Belli et al. 2014). This source is blended with the quiescent galaxy in all public photometric catalogs we explored (Whitaker et al. 2011; Muzzin et al. 2013a; Skelton et al. 2014; Laigle et al. 2016), although the large velocity offset measured with our CO spectra suggests it is a separate system (although likely to merge in future). Moreover, the high-resolution HST data indicate that the companion source may itself be a blend of three clumps or different satellite galaxies (see the inset in Figure 2). However, the components are unresolved at the low spatial resolution of our ALMA data and the CO line does not show evidence of multiple components.

We therefore extracted the flux density of ID = 1 through the deblending code Mophongo (Labbé et al. 2006, 2010a, 2010b, 2013, 2015). Briefly, this tool leverages a higher-resolution map to reconstruct the brightness profiles, and remove the contribution, of all sources within a radius of $9''$ from the source of interest. Aperture photometry is then performed on the neighbor-clean stamp, and corrected to total using the brightness profile on the low-resolution image and the point-spread function reconstructed at the specific location of the

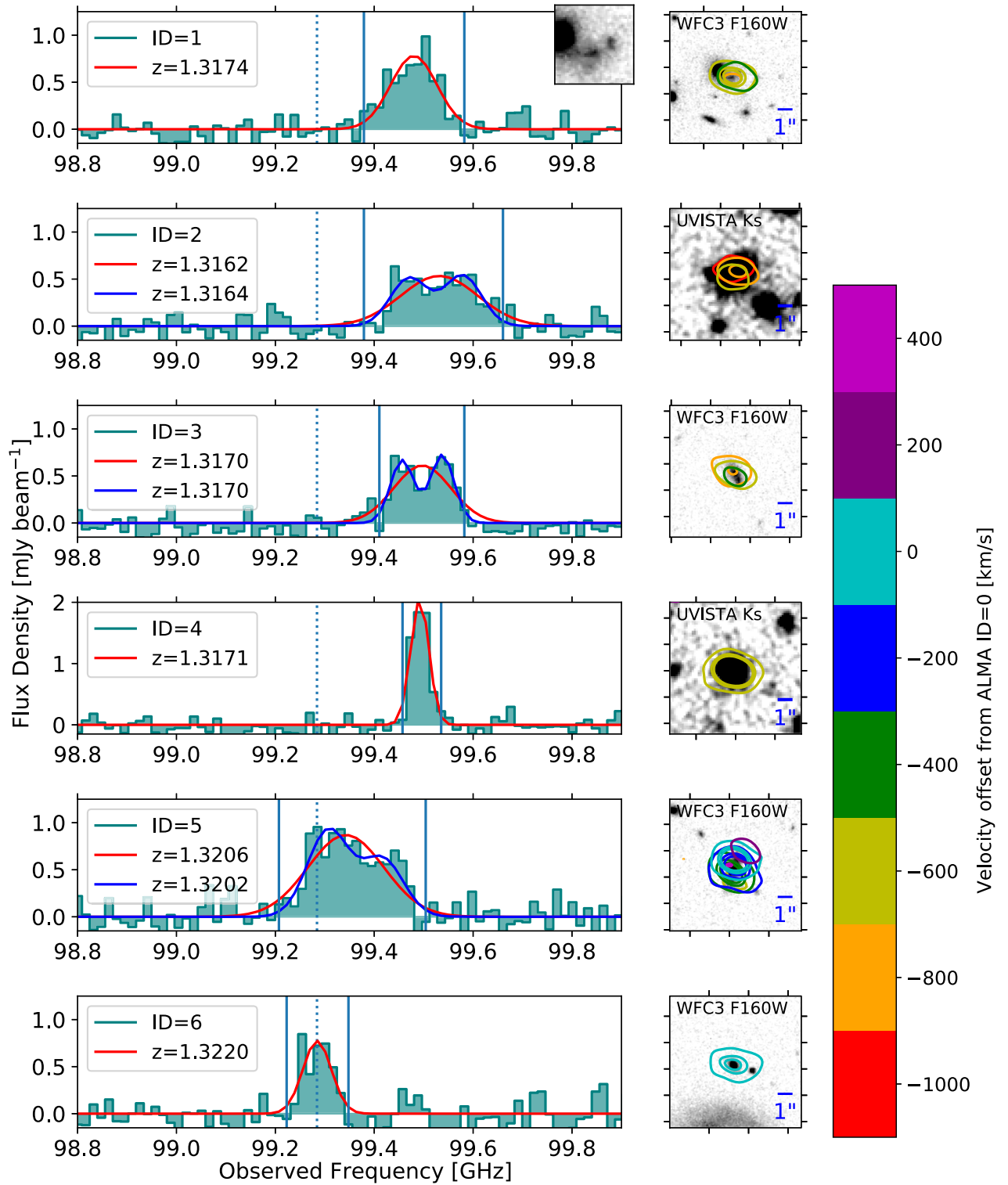


Figure 2. Left panel: our ALMA CO(2–1) spectra for the six emitters in 50 km s^{−1} channels. The dashed line corresponds to $z = 1.322$, the redshift of the quiescent galaxy target from (Williams et al. 2021). Red lines are single Gaussian fits to the spectra and blue are double Gaussian (redshifts as measured from each in the legend). The subpanel shown for ID = 1 is a zoom-in of the WFC3/F160W image showing the substructure that is blended in all catalogs (see Figure 4) with the primary quiescent galaxy (ID = 0). Right panel: near-IR image cutouts of each source, with ALMA contours overplotted. ALMA beam size is shown as the blue ellipse in top right panel. Contours are measured in 200 km s^{−1} channels and correspond to 25, 50, and 60 mJy beam^{−1} km s^{−1} levels and are color-coded by velocity offset relative to the systemic velocity of our target, ID = 0. This cluster lies on the edge of existing HST/WFC3 F160W imaging from CANDELS. UltraVISTA Ks band imaging is used for those galaxies without HST coverage.

target. For our analysis, we adopted the combined F125W, F140W, and F160W mosaics from the 3D-HST program (Skelton et al. 2014; Momcheva et al. 2016) as high-resolution

prior, and extracted the flux density using a 1¹/₈ diameter aperture. Given the low spatial resolution of the CO map, we forced the extraction of the photometry for ID = 1 by placing a

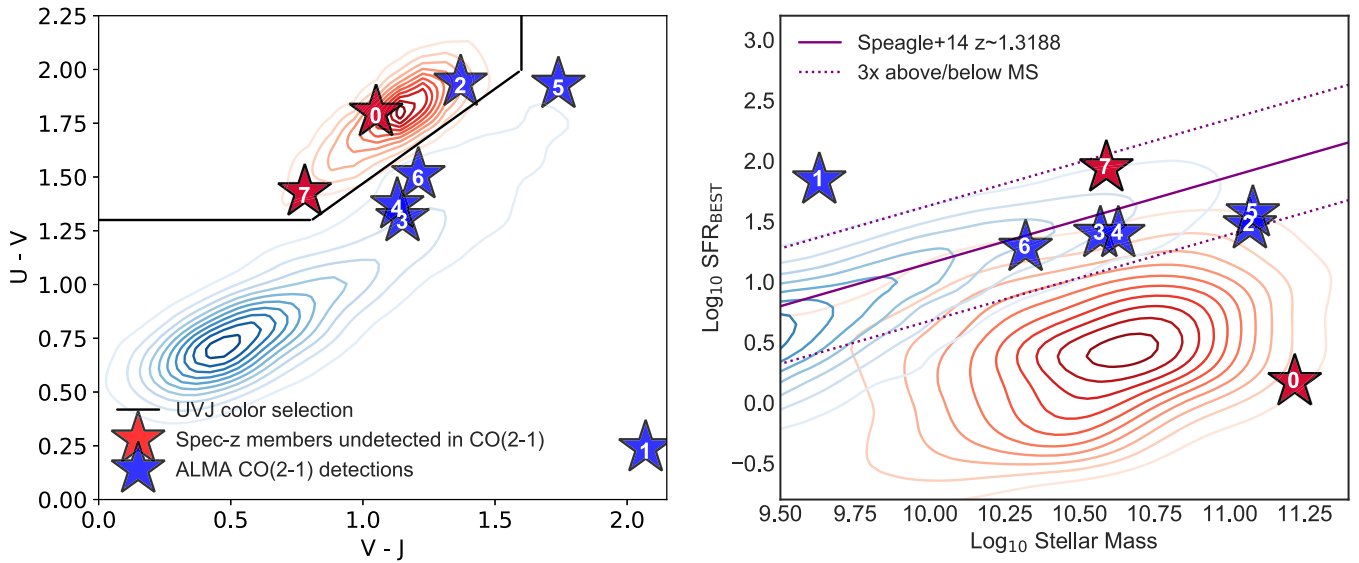


Figure 3. Properties measured by BAGPIPES for CO(2–1) emitters plus the two spectroscopically confirmed cluster members for which we have a CO(2–1) upper limit. The left panel shows restframe $U - V$ vs. $V - J$ colors for star-forming and quiescent 3D-HST galaxies (blue and red contours, respectively) at $1 < z < 1.5$. UVJ colors for our spectroscopically confirmed cluster members are measured with BAGPIPES. Right panel: the star formation– M^* diagram, with the main sequence as measured by Speagle et al. (2014). For 3D-HST galaxies, we use $\text{SFR}_{\text{UV+IR}}$. For our sample we use SFR_{best} as defined as in Table 1. Points are labeled by their ALMA ID.

synthetic point-source at the location corresponding to the peak of the CO emission. Specifically, we extracted the photometry in the CFHTLS (Erben et al. 2009; Hildebrandt et al. 2009) u^* , g , r , i , and z bands, Subaru/Suprime-Cam B_j , V_j , g^+ , r^+ , i^+ and z^+ (Taniguchi et al. 2007), Subaru HyperSuprimeCam g , r , i , z , and y (Aihara et al. 2018a, 2018b, 2019), Y , J , H , and K_s from the DR4 of the UltraVISTA program (McCracken et al. 2012), IRAC 3.6 and 4.5 μm from S-CANDELS (Ashby et al. 2015), and IRAC 5.8 and 8.0 μm from the S-COSMOS project (Sanders et al. 2007).

Given the lack of evidence of multiple independent galaxies based on the CO(2–1) line profile emitted from ID 1, we assume all optical/IR components make up a single companion at the same systemic velocity. We note that the fainter two of the deblended optical/near-IR clumps display bluer colors than the brightest primary component of the companion, possibly caused by patches of unobscured star formation within the source. The brightest primary component is very red, and lacks any detectable flux blueward of WFC3/F160W.

For results presented herein, we re-fit the UV to near-IR photometry from the UltraVISTA catalog for IDs 2–7, and our deblended photometry for IDs 0–1, uniformly using the spectral energy distribution (SED)-fitting code Bayesian Analysis of Galaxies for Physical Inference and Parameter ESTimation (BAGPIPES) (Carnall et al. 2018). BAGPIPES assumes the stellar population synthesis models of Bruzual & Charlot (2003) and implements nebular emission lines following the methodology of Byler et al. (2017) using the CLOUDY photoionization code (Ferland et al. 2017). We fit the photometry of our sample assuming a delayed τ -model star formation history (where prior limits range between 0.03 Gyr and the age of the universe at $z = 1.3$, and the exponential decline timescale τ ranges over 0.1–100 Gyr), and the Charlot & Fall (2000) dust attenuation model, to measure the stellar mass, SFR integrated over the last 100 Myr (SFR_{SED}), and rest-frame $U - V$ versus $V - J$ colors, for classifying galaxies as star-forming or quiescent (Williams et al. 2009; Muzzin et al. 2013b). The location of our spectroscopically confirmed cluster

members in the UVJ diagram is shown in the left panel of Figure 3.

We note that the spatially non-uniform colors in the deblended companion source (ID = 1) result in unusual integrated blue $U - V$ and red $V - J$ restframe colors. We tested SED-fitting the individual deblended clumps of ALMA ID = 1 separately, finding that the blue clumps have $>10\times$ lower stellar mass than the primary red source alone. Since they contribute only a tiny fraction of the overall mass (and we derive its SFR from the radio; see Section 2.4) our results do not depend on whether we assume the blue clumps belong to the primary source or not, besides producing the odd $U - V$ versus $V - J$ colors. Given the strange colors of ID = 1 we also explore a uniform prior range in metallicity, as well as fixing metallicity to solar. As this does not change our results (stellar masses are all consistent), we present results with metallicity fixed at solar. The SED-fitting results used in this work are listed in Table 1.

2.4. Star Formation Rates

We use the deep multi-wavelength data from mid-IR to radio in COSMOS to quantify and compare the SFRs for our CO-detected and non-detected sources. Unfortunately, given the proximity of source 0 (the central quiescent galaxy) and source 1, we are unable to use any published SFRs for these two sources, as they are blended in the ULTRAVISTA, 3DHST, and VLA 3 GHz radio catalogs (Muzzin et al. 2013a; Skelton et al. 2014; Smolčić et al. 2017; Algera et al. 2020). However, our CO spectroscopy in combination with the rest-optical spectroscopy of Belli et al. (2014) confirms that they are distinct sources (see the dotted line in Figure 2). Though blended in available radio catalogs (Smolčić et al. 2017; Algera et al. 2020), we confirm visually that two distinct radio sources are identifiable with the $0''.75$ resolution from the VLA-COSMOS 3 GHz Large Project (Smolčić et al. 2017). Leveraging our use of these spectroscopic priors, we perform source detection and photometry on the 3 GHz map using the

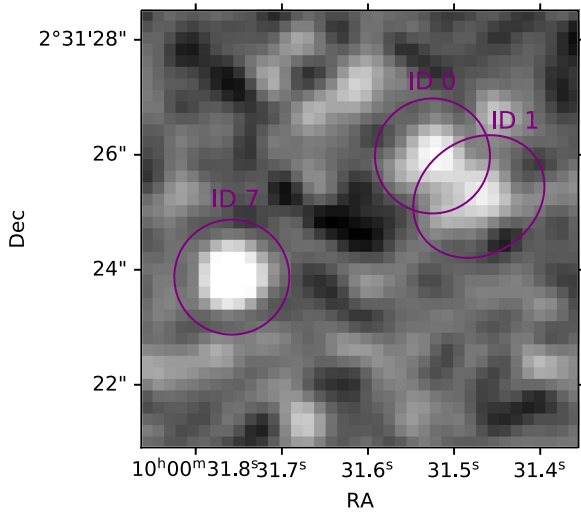


Figure 4. Radio image from the high-resolution (0.775) VLA-COSMOS 3 GHz Large Project (Smolčić et al. 2017) demonstrating IDs 0 and 1 are distinct radio sources, although blended in existing public catalogs. Our deblended radio fluxes for IDs 0 and 1 are presented in Section 2.4.

Python Blob Detection and Source Finder (PyBDSF) software package (v1.9.2; Mohan & Rafferty 2015), modeling sources as Gaussians with conservative source detection parameters ($\text{thresh_isl}=3.0$, $\text{thresh_pix}=5.0$). To deblend our sources, we turn off the grouping of nearby Gaussians into islands ($\text{group_by_isl}=\text{False}$), which yields separate detections at moderate significance (see Figure 4). We confirm that the deblended source fluxes total to the published blended flux within the uncertainties ($38.6 \pm 2.9 \mu\text{Jy}$; Smolčić et al. 2017).

The quiescent galaxy (source 0) is both a radio source, deblended by our radio photometry, and a blended $24 \mu\text{m}$ source. Given its quiescent nature as confirmed by spectroscopy (Belli et al. 2014), this likely indicates significant active galactic nucleus (AGN) activity, which cannot be disentangled from any SFR activity using the UV+IR SFR based on $24 \mu\text{m}$ (measured by Muzzin et al. 2013a) or the deblended radio flux. Instead, in line with current philosophy in the literature that SED-fit-based SFRs are less likely to be contaminated by AGNs among quiescent galaxies (e.g., Fumagalli et al. 2014), we use the SFR averaged over the last 100 Myr as measured with BAGPIPES (see Section 2.3).

For source 1, we use the deblended 3 GHz flux and k-correct to 1.4 GHz assuming the convention $S_\nu \propto \nu^\alpha$ with $\alpha = -0.7$ (Condon 1992). ALMA sources 2, 3, 4, and 5 are detected in the deeper radio imaging from Algera et al. (2020) and we use the k-corrected $L_{1.4 \text{ GHz}}$ from their public catalog to derive radio SFRs using the calibration

$$\log\left(\frac{\text{SFR}}{M_\odot \text{ yr}^{-1}}\right) = 0.823 \times \log\left(\frac{L_{1.4}}{\text{W Hz}^{-1}}\right) - 17.5 \quad (1)$$

from Molnár et al. (2021), which incorporates the luminosity dependence of the radio–IR correlation.

Source 2 is undetected at $24 \mu\text{m}$ (used to measure UV+IR SFR) and therefore we adopt its radio-derived SFR of $29 M_\odot \text{ yr}^{-1}$, which is just below the sensitivity level of MIPS $24 \mu\text{m}$. However, we note that its SFR derived from SED-fitting to the optical/near-IR data suggests a factor of ~ 3 lower SFR, in line with its measured red UVJ colors. Since the source

is not radio-loud, it is likely tracing the level of obscured star formation missed by SED-fitting and not an AGN. For sources 3, 4, and 5 the radio-derived SFR estimates are within a factor of $1.5\times$ those estimated based on UV+IR (Muzzin et al. 2013a). To maximize consistency among our sample we adopt the radio-based SFR for sources 1–5 herein.

Source 6 is undetected in any of the available radio imaging (Smolčić et al. 2017; Algera et al. 2020), and is undetected at $24 \mu\text{m}$, making its UV+IR SFR based on this photometry unreliable (Muzzin et al. 2013a). For this source we again use the SFR averaged over the last 100 Myr from BAGPIPES.

Source 7 (the spectroscopic source from Hasinger et al. 2018, without CO(2–1) emission) sits squarely in IRAC AGN color space (Donley et al. 2012; Kirkpatrick et al. 2013) and is also a radio and X-ray source. As such, its UV+IR SFR derived using MIPS is likely overestimated (it is $40\times$ over the SED-fit SFR and $2.5\times$ that from radio). However, the source is not radio-loud because it lies on the radio–IR correlation (Helou et al. 1985; Condon et al. 1991; Yun et al. 2001) and thus the majority of radio flux most likely arises from star formation rather than the AGN (Alberts et al. 2020). For this source as well we thus adopt the radio-based SFR ($87 M_\odot \text{ yr}^{-1}$) as with sources 1–5. We note that the SFR averaged over the last 100 Myr derived from SED-fitting suggests a lower SFR $\sim 5 M_\odot \text{ yr}^{-1}$, which is more in line with its red UVJ colors near the post-starburst region of the diagram (Belli et al. 2019), but the source would remain within the scatter of the main sequence (see Figure 3).

Our determined best estimates of the SFR as outlined above for each source (SFR_{best}) that is used in our analysis are quoted in Table 1. Based on these properties, six out of eight of our sample would be classified as main-sequence galaxies (Speagle et al. 2014; Whitaker et al. 2014; see the right panel of Figure 3). Source 0 is well below the main sequence and its companion source 1 lies above the main sequence.

2.5. Summary of Cluster Members

A total of 14 photometric candidate group members were identified by Gozaliasl et al. (2019) ranging from $1.29 < z_{\text{phot}} < 1.35$. Nine of those 14 are within the 20% ALMA primary beam area of our observations. Our target quiescent galaxy (source 0) spectroscopically confirmed by Belli et al. (2014) was not identified as a group member because their spectroscopic redshifts were not included in the public COSMOS catalogs. With our new data, we spectroscopically confirm three photometric cluster members identified by Gozaliasl et al. (2019) (the other six that are within our primary beam are undetected, including source 7). The other three CO sources were not identified as cluster members using the Laigle et al. (2016) catalog, but photometric redshifts from Muzzin et al. (2013a) place the galaxies within $\delta z \pm 0.1$ of the cluster redshift. As source 1 was absent from optical/IR and radio catalogs in COSMOS, it was not identified as a cluster member in the Gozaliasl et al. (2019) catalog. Eight spectroscopic members are now confirmed; all sources have spectroscopic redshifts that are within a range of $< 725 \text{ km s}^{-1}$.

Given our new spectroscopic confirmations, we use these redshifts to re-calculate the cluster redshift and velocity dispersion using the bi-weight location method described in Beers et al. (1990) using the astropy stats function `biweight_location` (Astropy Collaboration et al. 2013). We find a systemic redshift of $z=1.3188$ (with a dispersion of

$dz = 0.00245$ or 317 km s^{-1}) essentially the same as that listed by Gozaliasl et al. (2019) in the cluster redshift catalog (which was based only on the single spectroscopically confirmed galaxy in their data, source 7, with a redshift of $z = 1.319$). Following Danese et al. (1980), we correct for the contribution to the velocity dispersion introduced by the measurement uncertainty (assuming the typical redshift uncertainty of our ALMA data, 0.0001) and find a corrected value of $\sigma_v = 295 (+128, -55) \text{ km s}^{-1}$ where these are the $\pm 68\%$ uncertainties. This is consistent with that derived using the X-ray (360 km s^{-1}), and therefore we adopt the X-ray dispersion in the next section.

3. Results

3.1. Accretion Histories of Cluster Members

This overdensity of CO emitters is found in a relatively compact projected area on the sky. All eight spectroscopic members lie within the projected virial radius ($R_{200} \sim 50''$; $\sim 400 \text{ kpc}$). To explore their spatial distribution within the cluster and estimate the cluster accretion histories for each galaxy, we produce a phase-space diagram showing the velocities of the eight cluster members relative to the cluster redshift (ΔV , normalized by cluster velocity dispersion, σ_v , which was measured by Gozaliasl et al. (2019) using scaling relations for $L_x - M_{200}$ and $L_x - \sigma$; (e.g., Leauthaud et al. 2010; Connelly et al. 2012) versus the galaxy projected distance from the X-ray-derived cluster center (normalized by virial radius; R/R_{200}). Simulations indicate that using projected distances and line-of-sight velocities instead of full 3D space still results in accurate characterization in phase space (e.g., Rhee et al. 2017).

The phase space diagram is shown in Figure 5, where the curves delineate the approximate regions where galaxies would be considered in the central core of the cluster, recently accreted, or still infalling. We delineate regions according to $(R/R_{200}) \times (\Delta v/\sigma_v) < 0.2$ (cluster center), $0.2 < (R/R_{200}) \times (\Delta v/\sigma_v) < 1.35$ (intermediate and recently accreted regions), and $(R/R_{200}) \times (\Delta v/\sigma_v) > 1.35$, beyond which galaxies are still in their initial infall. These definitions of phase space regions are as outlined in both Noble et al. (2016) and Hayashi et al. (2017). We additionally plot a representation of the virialized region as defined in Mahajan et al. (2011) and Jaffé et al. (2015), approximated as a triangle with $|R| < R_{200}$ and $\Delta v < 1.5\sigma$. However, we note that these regions should be regarded as approximate since regions defined in projected phase space can contain interlopers (Rhee et al. 2017). Additionally, Gozaliasl et al. (2019) report relatively low signal-to-noise ratio (S/N) on the measured X-ray luminosity and halo mass for this cluster, 3.3 and 5.4 respectively, which corresponds to low S/N on the derived virial radius and velocity dispersion. However, we note that the X-ray derived values agree well with our spectroscopically derived cluster properties, as described in Section 2.5.

Given the wide bandwidth of the CO spectroscopy ($\sim 5500 \text{ km s}^{-1}$) we are sensitive to the overwhelming majority of possible velocities within the cluster center ($-7 < \Delta V/\sigma_v < 5$). Given our deep integration and the compact nature of this cluster, we probe 90% of the area within the virial radius ($R/R_{200} < 0.9$) within 20% of the ALMA primary beam to a 5σ limit of $M_{\text{H}_2} > 4.2 \times 10^{10} M_\odot$. While we do not detect any conclusively infalling CO sources, our data do not probe a substantial part of the first

infall region, which can stretch 2–3 times the size of the virial radius (e.g., Rhee et al. 2017; Zinger et al. 2018).

As mentioned previously, caution is advised when interpreting phase space diagrams, since the correspondence between the denoted regions and physical accretion histories is approximate, with interlopers possible in each given space (Rhee et al. 2017). This makes the interpretation of small samples such as ours difficult. As such, we focus our comparison with other samples in the literature in order to place it in the context of these earlier CO studies. Relatively few clusters currently have molecular gas constraints at $z \sim 1-2$ (Noble et al. 2017, 2019; Rudnick et al. 2017) and, in addition, well measured cluster parameters (Hayashi et al. 2017, 2018). Hayashi et al. presented the largest sample of molecular gas in phase space in a coeval ($z = 1.46$) but more massive X-ray cluster. In general, we find that our cluster galaxies occupy the same phase space as the Hayashi et al. sample, mostly populating the recently accreted/intermediate region with some galaxies in the cluster core (Figure 5). Our relative distribution between these two regions is in general agreement with the conclusion from Hayashi et al. that fewer CO detections are found in the cluster cores compared to the intermediate/recently accreted region. This could be an indication of a relative depletion of gas in the core, but our limited sample size precludes us from making any conclusive statement. While Hayashi et al. (2017) have narrowband O II imaging to identify galaxies which lack CO detections, we are unfortunately not spectroscopically complete enough to estimate the fraction of cluster members that have already lost the majority of molecular gas. We note the caveat that the core region is defined relative to the X-ray center, and therefore our designation of location within the cluster is approximate and assuming the cluster does not have significant sub-structure or asymmetries.

3.2. Comparison to Gas Properties of Field Galaxies

We expand this comparison by looking at the gas content in these cluster galaxies relative to that expected in coeval field galaxies. In Figure 5, we color-code galaxies in the phase space diagram using their deviation from the molecular gas fraction $f_{\text{H}_2} \equiv \frac{M_{\text{H}_2}}{(M_{\text{H}_2} + M^*)}$ predicted by the field scaling relations presented in Tacconi et al. (2018) such that

$$\Delta f_{\text{H}_2} = \frac{f_{\text{H}_2, \text{measured}}}{\langle f_{\text{H}_2, \text{field}}(z, \Delta MS, M^*) \rangle}. \quad (2)$$

where ΔMS is the deviation (in log space) from the star-forming main sequence as defined by Speagle et al. (2014). We bin the colorbar such that orange ($-0.2 < \text{Log}_{10} \Delta f_{\text{H}_2} < 0.2$ dex) corresponds to the range of systematic uncertainties in the molecular gas measurements that were used to build the scaling relation (Tacconi et al. 2020). We consider this range in orange to be consistent with the field-calibrated scaling, $\text{Log}_{10} \Delta f_{\text{H}_2} = 0$ (i.e., field-like). Although we note that Tacconi et al. (2018, 2020) do not characterize or quantify the scatter of the data used to measure the scaling relation, Liu et al. (2019) confirm that a range of 0.15–0.25 dex conservatively represents the typical systematic uncertainties and is also comparable to the scatter of molecular gas measurements at these redshifts.

We also color code the Hayashi et al. (2018) points by their deviation from the field main-sequence relations. Their work used a metallicity-dependent α_{CO} conversion factor

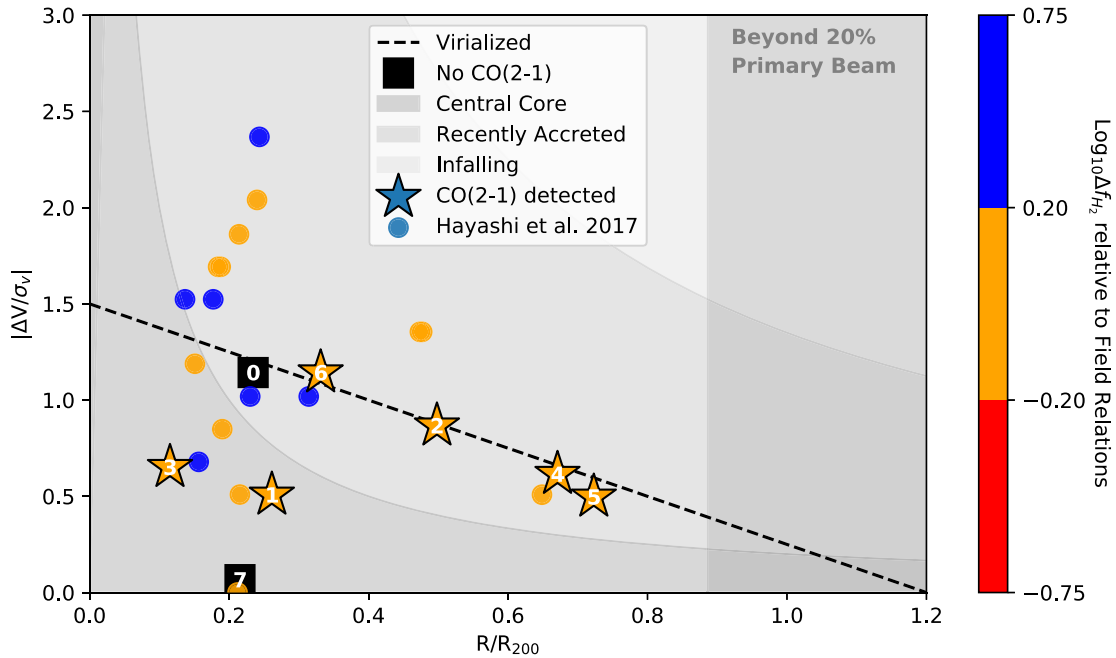


Figure 5. Phase diagram indicating accretion history of cluster galaxies. Galaxies are classified by their relative velocity to the cluster redshift (scaled by velocity dispersion of cluster) vs. their distance from the X-ray-derived cluster center, normalized by virial radius. Shaded curves delineate regions as defined in Noble et al. (2016) and Hayashi et al. (2017) for central core, recently accreted (defined here to include their intermediate region) and infall region. All spectroscopic sources are within the virial radius $R_{200} = 50.8$ arcsec = 425 kpc and are likely virialized. Area of phase space not probed by our data (beyond 20% of the primary beam limit; $\sim 45''$; $M_{\text{H}_2} > 4.2 \times 10^{10} M_{\odot}$ at 5σ) is indicated by the gray box ($R/R_{200} > 0.9$). Our spectral coverage (~ 5500 km s $^{-1}$ bandwidth) limits lie off the plot at -5 and $+7$ on the y-axis. The dashed line represents the virialized region as defined in Mahajan et al. (2011) and Jaffé et al. (2015). For comparison, we include comparable data from a virialized, coeval but more massive ($z = 1.46$, $\text{Log}_{10} M_{\text{halo}}/M_{\odot} \sim 14$ cluster (Hayashi et al. 2017, 2018). Both data sets indicate that gas survives in galaxies after first infall, and can even maintain field-like gas reservoirs within the core or virialized region.

(Genzel et al. 2012). To ensure a fair comparison to our work, we re-calculate M_{H_2} from their measured L'_{CO} using our assumed $r_{21} = 0.8$ and $\alpha_{\text{CO}} = 4.4$, consistent with the value commonly adopted for field scaling relations (Tacconi et al. 2020). Using the re-calculated values, we then measure f_{H_2} and compare to the field scaling relations. We find that the majority (65%) of the Hayashi et al. (2017, 2018) CO-detected galaxies are consistent with field-like gas content, and 35% of CO-detected galaxies are in excess of field expectations (i.e., gas enhanced).

In contrast, all of our CO detections have gas fractions that are consistent within the scatter of field-based scaling relations at similar SFR and M^* (median $\text{Log}_{10} \Delta f_{\text{H}_2} = 0.05$ dex). Of the two CO undetected galaxies, their limits suggest very low gas content, consistent with their *UVJ* quiescent status. We additionally note that our conclusions would not change had we adopted a metallicity-dependent α_{CO} for our lowest-mass (and therefore presumably lowest-metallicity) source ID = 1, whose inferred f_{H_2} would still be consistent with the field relations.

We next expand our comparison¹¹ to include the sample of CO detections in $z \sim 1.6$ cluster galaxies presented in Noble et al. (2017, 2019). As their molecular gas measurements were made with similar assumptions as this work, no modifications

are made. In Figure 6, we present the H_2 masses based on CO detections for coeval cluster galaxies at $z \sim 1-2$, along with the detection limits (5σ at 50% of the ALMA primary beam) for each work ($M_{\text{H}_2}^{\text{lim}} \sim 6.5 \times 10^{10}$ and $7.6 \times 10^{10} M_{\odot}$ for Noble et al. 2017 and Hayashi et al. 2018, respectively). Our 5σ detection limit at 50% the primary beam ($1.6 \times 10^{10} M_{\odot}$) is nominally 4–4.5 times deeper than that of Noble et al. (2017) and Hayashi et al. (2017, 2018), though overlap in multiple pointings in the latter survey probe lower M_{H_2} in small areas. Noble et al. (2019) presented data of similar depth to this work ($M_{\text{H}_2}^{\text{lim}} \sim 1.95 \times 10^{10} M_{\odot}$) over a single pointing, detecting four new galaxies as compared to the Noble et al. (2017) observations.

Overall, the CO detections in this work sit at relatively lower gas masses compared to previous works. Our data further put strong upper limits on our two CO-undetected cluster members, with gas masses less than $5.5 \times 10^9 M_{\odot}$. Incomplete spectroscopy in the optical/IR, however, prevents us from ruling out more gas-poor cluster members. To explore this issue, we compare to a recent study of molecular gas using stacking of dust continuum measurements in 11 massive clusters at $z \sim 1-2$ (Alberts et al. 2022). In field galaxies, CO and dust continuum yield comparable measurements of the molecular gas (Tacconi et al. 2020); differences may exist in overdense environments, but this issue has only been explored in small samples of proto-cluster galaxies (e.g., Lee et al. 2021). For now, we assume they are comparable within the uncertainties of this study. In the mass bin most comparable to this work ($\text{Log}_{10} M^*/M_{\odot} \sim 10.75$), Alberts et al. (2022) found that the average molecular gas in cluster galaxies sits at $1.6 \times 10^{10} M_{\odot}$, right at our 5σ detection limit. At higher masses, the average gas mass may be above our detection limit; however, the small area

¹¹ Molecular gas constraints also exist for galaxies in overdensities or proto-clusters at $z > 2$ (Dannerbauer et al. 2017; Lee et al. 2017; Umehata et al. 2017; Oteo et al. 2018; Wang et al. 2018; Castignani et al. 2019; Gómez-Guijarro et al. 2019; Zavala et al. 2019; Long et al. 2020; Champagne et al. 2021; Hill et al. 2020, 2021; Jin et al. 2021; Shen et al. 2021), as well as some unconfirmed candidate clusters and structures at $z < 2$ (Aravena et al. 2012; Kneissl et al. 2019). However given that proto-clusters are likely to be characterized by significantly different dynamical states than a relaxed, virialized cluster, we do not directly compare to them.

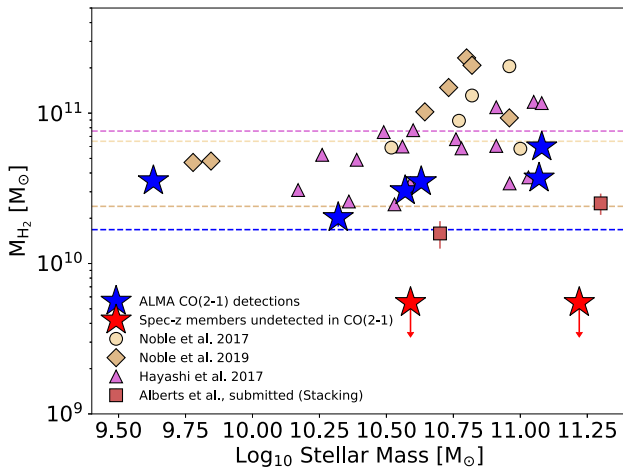


Figure 6. Molecular gas mass as a function of stellar mass for cluster studies at $z \sim 1-2$. Our CO(2-1)-detected cluster members are shown as blue stars. Spectroscopic, but CO-undetected members are shown as upper limits as red stars. Cluster galaxies detected in CO at $z \sim 1.5$ are shown as purple triangles (Hayashi et al. 2017, 2018) and at $z \sim 1.6$ as light yellow circles (Noble et al. 2017) and dark yellow diamonds (Noble et al. 2019). The 5σ detection limit at 50% of the ALMA beam is shown as dashed lines with corresponding colors; Hayashi et al. (2017, 2018) and Noble et al. (2017) have limits roughly $4.5\times$ shallower than this work, while Noble et al. (2019) presented follow-up at similar depth. We note that the Hayashi et al. (2017) ALMA mosaic includes overlapping pointings, resulting in small areas deeper than the representative limit. A dust continuum stacking study (Alberts et al. 2022) is shown for contrast as brown squares, representing the average gas masses of undetected $z \sim 1-2$ star-forming cluster galaxies.

covered may be insufficient to observe these rarer, more massive galaxies. This comparison suggests that gas-poor cluster members may still be missing from studies of detected galaxies, even given the deep detection limits presented in this work.

To put the gas properties of these $z \sim 1-2$ cluster galaxies in the context of the field, we derive the field-relative gas depletion timescales and gas fractions (Figure 7) by dividing by the predicted values via the Tacconi et al. (2018) scaling relation, as described for Figure 5. The predicted field values are calculated using the redshift, stellar mass, and distance from the main sequence (ΔMS) of each cluster galaxy, providing a direct comparison. The scatter in $\tau_{\text{depl}}/\tau_{\text{depl}}^{\text{field}}$ is taken to be 0.3 dex as in Liu et al. (2019), incorporating measurement and systematic uncertainties in the gas masses and measured SFRs. The scatter in $f_{\text{H}_2}/f_{\text{H}_2}^{\text{field}}$ is adopted as 0.2 dex, assuming that the scatter in the ratio is dominated by the uncertainties in the gas masses rather than by systematic errors in the stellar mass measurements. Our deep detection limit enables us to probe the entire main sequence at $\text{Log}_{10} M^*/M_{\odot} > 10.5$ down to gas masses of $M_{\text{H}_2} \gtrsim 1.6 \times 10^{10} M_{\odot}$, from which we can safely rule out the presence of cluster galaxies with extended gas depletion timescales or enhanced gas fractions, out to $R/R_{200} > 0.2$ and $\Delta v/\sigma_v > 1.5$. This is in contrast to existing CO surveys which find enhanced gas content (e.g., $M_{\text{H}_2} > 6 - 8 \times 10^{10} M_{\odot}$), with the corresponding potential for long depletion timescales, modulo uncertainties in SFR measurements, and enhanced gas fractions in excess of the field. These gas-enhanced members are even found in the cluster cores and the virialized regions (Hayashi et al. 2017, 2018; see Figure 5). On the other hand, the stacked average gas properties of star-forming cluster members at $z \sim 1-1.75$ (Alberts et al. 2022), probing below current detection limits, suggest shorter depletion timescales

and lower gas fractions, below the field scaling relations at fixed stellar mass and distance from the main sequence, are still missing from these analyses. We discuss this possibility further in Section 4.

Finally, we note that both sources 0 and 7, which lie in the quiescent region of *UVJ* color space and are likely in the cluster core, have low limits on any molecular gas fractions (<3 and $<12\%$, respectively), in line with accumulating evidence that quiescent galaxies have cold molecular gas reservoirs of order a few percent or less (Bezanson et al. 2019; Caliendo et al. 2021; Whitaker et al. 2021; Williams et al. 2021). However, both of these sources are detected at $24 \mu\text{m}$ and 3 GHz. They are similar to the sample studied by Belli et al. (2021) in that they were selected for a quiescent optical/near-IR SED, but have relatively bright emission at $24 \mu\text{m}$. By contrast, Belli et al. (2021) finds diverse gas reservoirs that are substantially higher f_{H_2} (13%–23%) for similar IR-bright quiescent galaxies (although they do not have IRAC colors reflective of AGNs, such as our source 7). The number of such sources with measured gas reservoirs is small and thus we cannot reach definitive conclusions, but it is interesting that our two *UVJ*-quiescent, non-detected cluster members exhibit substantially lower gas reservoirs in contrast to Belli et al. (2021).

4. Discussion and Conclusions

In this work, we have presented a serendipitous discovery of CO emitters in the central core and recently accreted regions of phase space in a low-mass ($\text{Log}_{10} M_{\text{halo}}/M_{\odot} = 13.6$) cluster at $z = 1.3188$. These ultra-deep ALMA data provide evidence that molecular gas survives first infall into the cluster environment, and even maintains field-like gas content in main-sequence galaxies (for all six CO-detected sources). An additional two members spectroscopically confirmed via optical/IR spectroscopy are not detected in CO(2-1), indicating gas loss consistent with the evidence that they are in a more evolved, quiescent state.

Despite these deep data, however, we do not find evidence for enhanced gas content within $\sim 90\%$ of the virial radius. This result differs from comparable CO studies of coeval clusters at $z \sim 1-2$. Where gas is detected, these studies mostly find that cluster members have gas reservoirs consistent with the field (e.g., Rudnick et al. 2017; see also Castignani et al. 2018 who estimate field-like gas content for two main-sequence cluster galaxies blended in CO). But some have also found a significant fraction of members hosting elevated gas content relative to the field scaling relations (in particular Hayashi et al. 2017, 2018 and Noble et al. 2017, 2019; see Figure 7). There are a few things to consider in interpreting this. First, it is important to note the differences in the relative sizes of the areas probed. Our survey is the smallest among Hayashi et al. (2017) and Noble et al. (2017), with only 1 ALMA pointing ($45''$ radius at 20% the primary beam). Comparatively, Noble et al. (2017) probe nearly $4\times$ this area, and Hayashi et al. (2017) nearly $1.5\times$, which may have increased the chances to catch rarer gas-enhanced sources.

Second, we point out that given that Noble et al. (2017, 2019), Rudnick et al. (2017) and Hayashi et al. (2017, 2018) provide some of the first constraints on CO in high-redshift cluster galaxies, the targets were chosen to be highly star-forming, and therefore likely containing large gas reservoirs, in order to maximize detection of CO rather than to create an unbiased sample. As a serendipitous detection, our

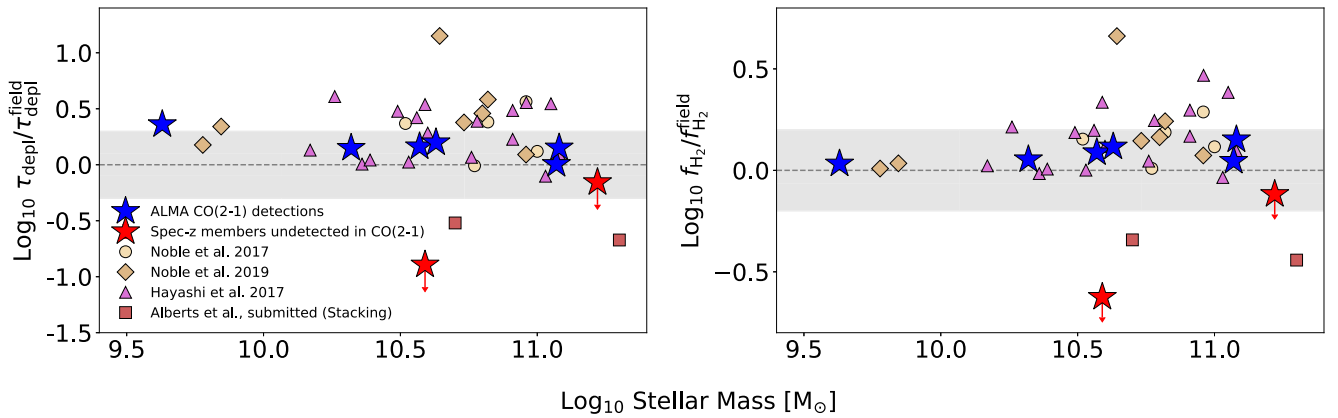


Figure 7. Gas depletion timescales (left) and gas fractions (right) of cluster galaxies relative to the predicted field gas properties as a function of stellar mass. The predicted field properties are derived for each individual source given its redshift, stellar mass, and distance from the Speagle et al. (2014) main sequence. Symbols are as in Figure 6. The dashed line represents the Tacconi et al. (2018) field scaling relation for τ_{depl} and f_{H_2} with an assumed scatter of 0.3 dex (Liu et al. 2019) for the former and 0.2 dex for the latter (shaded regions). As shown in Figure 6, our survey probes the entire main sequence at $\text{Log}_{10} M^*/M_{\odot} > 10.5$, one of the deepest limits to date. The CO detected cluster members in this work are consistent with field-like gas properties, while other CO studies (Hayashi et al. 2017, 2018; Noble et al. 2017; 2019) show a mix of galaxies on and above the field relations. Dust continuum stacking of star-forming galaxies (brown squares; Alberts et al. 2022), on the other hand, places the average gas depletion timescales and gas fractions at shorter and lower than the field scaling relations.

cluster is not biased in this way; however, even combined, these cluster studies are still in the regime of small-number statistics.

Given the caveats above, are these galaxies with enhanced gas content rare and unique among the more field-like cluster members? Interestingly, even those galaxies consistent with the field scaling relations remain within the upper envelope of the scatter. Given the relatively high detection limit of the earlier surveys, it is plausible that main-sequence populations of galaxies with lower gas content were simply missed. However, an interesting case is the deeper ALMA followup of one cluster in Noble et al. (2017) published by Noble et al. (2019). While Noble et al. (2019) achieved a depth more comparable to our data for the one cluster (see Figure 6), even this study found that the new CO detections among previously undetected lower-mass objects remain in the upper envelope of the scatter of the field scaling relations, in good agreement with the sources presented in this work. The reason for the perceived dearth of gas reservoirs below the field scaling relation (encompassing the lower envelope of the scatter), is not clear (see Figure 7), though we note that the deep Noble et al. (2019) coverage is currently only of a single $\sim 48''$ radius pointing (at 20% of the primary beam), and does not provide a uniform mapping over the entire cluster. In summary, from the small number of clusters surveyed, there appears to be some tentative evidence for systematically larger molecular gas reservoirs relative to the field in CO-detected sources (although see Coogan et al. 2018 for one counterexample at higher redshift), even if the systematic increase largely remains within the overall scatter of field galaxies. This may hint at a shared mechanism for the cluster members displaying enhanced gas fractions.

Wider surveys in a statistical sample of clusters to the depths presented here still might not be enough to present the full picture of molecular gas in cluster galaxies. There is emerging evidence from stacking of dust continuum emission that the cold gas reservoirs of star-forming cluster galaxies are, on average, actually depressed below the field scaling relations across redshifts. This has been seen at $z \sim 0.7$ (Betti et al. 2019), $z \sim 1-2$ (Alberts et al. 2022), and in $z \sim 2$ proto-cluster galaxies (Zavala et al. 2019). In Figure 7, we compare directly

to stacking results presented in Alberts et al. (2022) which looked at 126 star-forming galaxies of similar stellar mass, but in more massive clusters ($M_{\text{halo}} \sim 2-5 \times 10^{14} M_{\odot}$). This study found sub-field gas content out to $2R_{\text{vir}}$ over 11 similarly selected clusters, more effectively mitigating the impact of cluster-to-cluster variation and the potential biases in observing only a small portion the cluster environment (as we have here). While our cluster may be a special case (reflecting cluster-to-cluster variance), or it could be that lower-mass clusters such as ours retain more gas than the more massive clusters studied in Alberts et al. (2022), the puzzling difference is still present when comparing the current literature using CO and dust detections to stacking results. If the average gas mass is somewhere below the field, in a regime where gas has been lost relative to comparable field galaxies, where are the gas-deficient “sub-field” cluster members?

Unfortunately this regime of low gas content probed by stacking has not fully been reached by current CO surveys; the Alberts et al. (2022) results place the average gas mass at our relatively deep 5σ detection limit. Understanding the distribution of gas masses among cluster galaxies is key to constraining the mechanisms responsible for gas enhancement or gas loss, and will require detections probing below the predicted field levels of gas content over larger areas of the cluster environment. In combination, these studies further highlight the mystery of CO detections inhabiting the upper envelope of the field scaling relations.

Alongside additional observations, the large range in gas properties suggested by detection and stacking studies, plus the aforementioned cluster-to-cluster variation, stress the importance of simulations in interpreting small empirical samples. Recently, cosmological simulations have begun to address the question of gas properties in cluster environments. They find significant gas loss starting at large radii ($> 2R_{\text{vir}}$) ranging from the stripping of hot halo gas (Zinger et al. 2018) to the complete removal of all molecular gas (Arthur et al. 2019; Mostoghiu et al. 2021) by the first passage of the cluster core (see also Oman & Hudson 2016; Oman et al. 2021). In the first scenario, tightly bound disk gas is retained enough for star formation to proceed unimpeded for a time, consistent with the “delayed, then quenched” scenario proposed by Wetzel et al. (2013) and supported by subsequent





studies (Muzzin et al. 2014; Bahé & McCarthy 2015; Haines et al. 2015; Oman & Hudson 2016; Rhee et al. 2020; Cortese et al. 2021; see also Maier et al. 2019a, 2019b). Depending on the fraction of total gas removed by stripping, our field-like gas masses may be consistent with the removal of hot halo gas, while more extreme stripping may be supported by the stacking results. Populations with enhanced gas content are not well represented in these simulations; however, simulations have explored the idea of gas streams penetrating the cluster ICM (Zinger et al. 2016), which may provide a mechanism for delivering new gas to cluster galaxies such as has been plausibly observed at lower redshifts in BCGs (Castignani et al. 2020; Dunne et al. 2021).

Our new data make this cluster the lowest-mass cluster at $z > 1$ with both evidence of virialization and characterization of the molecular gas reservoirs. Thus, this study bridges the observational gap between gas properties of the most massive clusters during this epoch, and those in the field. More systematic surveys of molecular gas using deep CO or dust emission of clusters across halo mass are needed to constrain the physical processes impacting star formation activity during the critical cluster transition era of $1 < z < 2$.

We thank Ghassem Gozaliasl and Alexis Finoguenov for sharing their COSMOS group catalog, and Ivo Labbé for allowing use of the Mophongo software. C.C.W. and C.N.A.W. acknowledge support from NIRCAM Development Contract NAS5-02105 from NASA Goddard Space Flight Center to the University of Arizona. J.S. acknowledges support provided by NASA through NASA Hubble Fellowship grant #HF2-51446 awarded by the Space Telescope Science Institute, which is operated by the Association of Universities for Research in Astronomy, Inc., for NASA, under contract NAS5-26555. K.E.W. acknowledges funding from the Alfred P. Sloan Foundation grant No. FG-2019-12514. This paper makes use of the following ALMA data: ADS/JAO.ALMA #2018.1.01739.S. ALMA is a partnership of ESO (representing its member states), NSF (USA), and NINS (Japan), together with NRC (Canada), NSC and ASIAA (Taiwan), and KASI (Republic of Korea), in cooperation with the Republic of Chile. The Joint ALMA Observatory is operated by ESO, AUI/NRAO, and NAOJ. The National Radio Astronomy Observatory is a facility of the National Science Foundation operated under cooperative agreement by Associated Universities, Inc. The Cosmic Dawn Center is funded by the Danish National Research Foundation.

Software: NumPy (Harris et al. 2020), Matplotlib (Hunter 2007), Astropy (Astropy Collaboration et al. 2018), SciPy (Virtanen et al. 2020), Seaborn (Waskom 2021), CASA (McMullin et al. 2007) BAGPIPES (Carnall et al. 2018) uvmultifit (Martí-Vidal et al. 2014) CLOUDY (Ferland et al. 2017) PyBDSF (v1.2) (Mohan & Rafferty 2015) MOPHONGO (Labbé et al. 2006, 2010a, 2010b, 2013, 2015).

ORCID iDs

Christina C. Williams  <https://orcid.org/0000-0003-2919-7495>
 Stacey Alberts  <https://orcid.org/0000-0002-8909-8782>
 Justin S. Spilker  <https://orcid.org/0000-0003-3256-5615>
 Allison G. Noble  <https://orcid.org/0000-0003-1832-4137>
 Mauro Stefanon  <https://orcid.org/0000-0001-7768-5309>
 Christopher N. A. Willmer  <https://orcid.org/0000-0001-9262-9997>

Rachel Bezanson  <https://orcid.org/0000-0001-5063-8254>
 Desika Narayanan  <https://orcid.org/0000-0002-7064-4309>
 Katherine E. Whitaker  <https://orcid.org/0000-0001-7160-3632>

References

- Aihara, H., Arimoto, N., Armstrong, R., et al. 2018a, *PASJ*, 70, S4
 Aihara, H., AlSayyad, Y., Ando, M., et al. 2019, *PASJ*, 71, 114
 Aihara, H., Armstrong, R., Bickerton, S., et al. 2018b, *PASJ*, 70, S8
 Alberts, S., Adams, J., Gregg, B., et al. 2022, *ApJ*, 927, 235
 Alberts, S., Lee, K.-S., Pope, A., et al. 2021, *MNRAS*, 501, 1970
 Alberts, S., Pope, A., Brodwin, M., et al. 2014, *MNRAS*, 437, 437
 Alberts, S., Pope, A., Brodwin, M., et al. 2016, *ApJ*, 825, 72
 Alberts, S., Rujopakarn, W., Rieke, G. H., Jagannathan, P., & Nyland, K. 2020, *ApJ*, 901, 168
 Algera, H. S. B., van der Vlugt, D., Hodge, J. A., et al. 2020, *ApJ*, 903, 139
 Aravena, M., Carilli, C. L., Salvato, M., et al. 2012, *MNRAS*, 426, 258
 Arthur, J., Pearce, F. R., Gray, M. E., et al. 2019, *MNRAS*, 484, 3968
 Ashby, M. L. N., Willner, S. P., Fazio, G. G., et al. 2015, *ApJS*, 218, 33
 Astropy Collaboration, Price-Whelan, A. M., Sipőcz, B. M., et al. 2018, *AJ*, 156, 123
 Astropy Collaboration, Robitaille, T. P., Tollerud, E. J., et al. 2013, *A&A*, 558, A33
 Bahé, Y. M., & McCarthy, I. G. 2015, *MNRAS*, 447, 969
 Balogh, M. L., Schade, D., Morris, S. L., et al. 1998, *ApJL*, 504, L75
 Bayliss, M. B., Ashby, M. L. N., Ruel, J., et al. 2014, *ApJ*, 794, 12
 Beers, T. C., Flynn, K., & Gebhardt, K. 1990, *AJ*, 100, 32
 Belli, S., Contursi, A., Genzel, R., et al. 2021, *ApJL*, 909, L11
 Belli, S., Newman, A. B., & Ellis, R. S. 2014, *ApJ*, 783, 117
 Belli, S., Newman, A. B., & Ellis, R. S. 2019, *ApJ*, 874, 17
 Betti, S. K., Pope, A., Scoville, N., et al. 2019, *ApJ*, 874, 53
 Bezanson, R., Spilker, J., Williams, C. C., et al. 2019, *ApJL*, 873, L19
 Bolatto, A. D., Wolfire, M., & Leroy, A. K. 2013, *ARA&A*, 51, 207
 Brodwin, M., Stanford, S. A., Gonzalez, A. H., et al. 2013, *ApJ*, 779, 138
 Bruzual, G., & Charlot, S. 2003, *MNRAS*, 344, 1000
 Byler, N., Dalcanton, J. J., Conroy, C., & Johnson, B. D. 2017, *ApJ*, 840, 44
 Caliendo, J. N., Whitaker, K. E., Akhshik, M., et al. 2021, *ApJL*, 910, L7
 Carnall, A. C., McLure, R. J., Dunlop, J. S., & Davé, R. 2018, *MNRAS*, 480, 4379
 Casey, C. M. 2016, *ApJ*, 824, 36
 Castignani, G., Combes, F., Salomé, P., et al. 2018, *A&A*, 617, A103
 Castignani, G., Combes, F., Salomé, P., et al. 2019, *A&A*, 623, A48
 Castignani, G., Pandey-Pommier, M., Hamer, S. L., et al. 2020, *A&A*, 640, A65
 Champagne, J. B., Casey, C. M., Zavala, J. A., et al. 2021, *ApJ*, 913, 110
 Charlot, S., & Fall, M. 2000, *ApJ*, 539, 718
 Chatterjee, S., Ho, S., Newman, J. A., & Kosowsky, A. 2010, *ApJ*, 720, 299
 Chiang, Y.-K., Overzier, R., & Gebhardt, K. 2013, *ApJ*, 779, 127
 Chiang, Y.-K., Overzier, R. A., Gebhardt, K., & Henriques, B. 2017, *ApJL*, 844, L23
 Condon, J. J. 1992, *ARA&A*, 30, 575
 Condon, J. J., Anderson, M. L., & Helou, G. 1991, *ApJ*, 376, 95
 Connelly, J. L., Wilman, D. J., Finoguenov, A., et al. 2012, *ApJ*, 756, 139
 Coogan, R. T., Daddi, E., Sargent, M. T., et al. 2018, *MNRAS*, 479, 703
 Cooper, M. C., Newman, J. A., Croton, D. J., et al. 2006, *MNRAS*, 370, 198
 Cortese, L., Catinella, B., & Smith, R. 2021, *PASA*, 38, e035
 Danese, L., de Zotti, G., & di Tullio, G. 1980, *A&A*, 82, 322
 Dannerbauer, H., Lehnert, M. D., Emonts, B., et al. 2017, *A&A*, 608, A48
 Donley, J. L., Koekemoer, A. M., Brusa, M., et al. 2012, *ApJ*, 748, 142
 Dressler, A. 1980, *ApJ*, 236, 351
 Dunne, D. A., Webb, T. M. A., Noble, A., et al. 2021, *ApJL*, 909, L29
 Erben, T., Hildebrandt, H., Lerchster, M., et al. 2009, *A&A*, 493, 1197
 Fassbender, R., Nastasi, A., Böhringer, H., et al. 2011, *A&A*, 527, L10
 Fassbender, R., Nastasi, A., Santos, J. S., et al. 2014, *A&A*, 568, A5
 Ferland, G. J., Chatzikos, M., Guzmán, F., et al. 2017, *RMxAA*, 53, 385
 Finn, R. A., Desai, V., Rudnick, G., et al. 2010, *ApJ*, 720, 87
 Fumagalli, M., Labbé, I., Patel, S. G., et al. 2014, *ApJ*, 796, 35
 Geach, J. E., Smail, I., Ellis, R. S., et al. 2006, *ApJ*, 649, 661
 Genzel, R., Tacconi, L. J., Combes, F., et al. 2012, *ApJ*, 746, 69
 Genzel, R., Tacconi, L. J., Lutz, D., et al. 2015, *ApJ*, 800, 20
 Gómez-Guijarro, C., Riechers, D. A., Pavesi, R., et al. 2019, *ApJ*, 872, 117
 Gozaliasl, G., Finoguenov, A., Khosroshahi, H. G., et al. 2018, *MNRAS*, 475, 2787
 Gozaliasl, G., Finoguenov, A., Tanaka, M., et al. 2019, *MNRAS*, 483, 3545

- Haines, C. P., Pereira, M. J., Smith, G. P., et al. 2015, *ApJ*, 806, 101
- Hall, K. R., Zakamska, N. L., Addison, G. E., et al. 2019, *MNRAS*, 490, 2315
- Harris, C. R., Millman, K. J., van der Walt, S. J., et al. 2020, *Natur*, 585, 357
- Hasinger, G., Capak, P., Salvato, M., et al. 2018, *ApJ*, 858, 77
- Hayashi, M., Kodama, T., Kohno, K., et al. 2017, *ApJL*, 841, L21
- Hayashi, M., Kodama, T., Koyama, Y., Tadaki, K.-I., & Tanaka, I. 2011, *MNRAS*, 415, 2670
- Hayashi, M., Tadaki, K.-i., Kodama, T., et al. 2018, *ApJ*, 856, 118
- Helou, G., Soifer, B. T., & Rowan-Robinson, M. 1985, *ApJL*, 298, L7
- Hildebrandt, H., Pielorz, J., Erben, T., et al. 2009, *A&A*, 498, 725
- Hill, R., Chapman, S., Phadke, K. A., et al. 2021, arXiv:2109.04534
- Hill, R., Chapman, S., Scott, D., et al. 2020, *MNRAS*, 495, 3124
- Hilton, M., Lloyd-Davies, E., Stanford, S. A., et al. 2010, *ApJ*, 718, 133
- Hunter, J. D. 2007, *CSE*, 9, 90
- Jaffé, Y. L., Smith, R., Candlish, G. N., et al. 2015, *MNRAS*, 448, 1715
- Jin, S., Dannerbauer, H., Emonts, B., et al. 2021, *A&A*, 652, A11
- Kirkpatrick, A., Pope, A., Charmandaris, V., et al. 2013, *ApJ*, 763, 123
- Kneissl, R., Polletta, M. d. C., Martinache, C., et al. 2019, *A&A*, 625, A96
- Kravtsov, A. V., Vikhlinin, A., & Nagai, D. 2006, *ApJ*, 650, 128
- Kroupa, P. 2001, *MNRAS*, 322, 231
- Labbé, I., Bouwens, R., Illingworth, G. D., & Franx, M. 2006, *ApJL*, 649, L67
- Labbé, I., González, V., Bouwens, R. J., et al. 2010a, *ApJL*, 708, L26
- Labbé, I., González, V., Bouwens, R. J., et al. 2010b, *ApJL*, 716, L103
- Labbé, I., Oesch, P. A., Bouwens, R. J., et al. 2013, *ApJL*, 777, L19
- Labbé, I., Oesch, P. A., Illingworth, G. D., et al. 2015, *ApJS*, 221, 23
- Laigle, C., McCracken, H. J., Ilbert, O., et al. 2016, *ApJS*, 224, 24
- Leauthaud, A., Finoguenov, A., Kneib, J.-P., et al. 2010, *ApJ*, 709, 97
- Lee, M. M., Tanaka, I., Iono, D., et al. 2021, *ApJ*, 909, 181
- Lee, M. M., Tanaka, I., Kawabe, R., et al. 2017, *ApJ*, 842, 55
- Lewis, I., Balogh, M., De Propriis, R., et al. 2002, *MNRAS*, 334, 673
- Liu, D., Schinnerer, E., Groves, B., et al. 2019, *ApJ*, 887, 235
- Long, A. S., Cooray, A., Ma, J., et al. 2020, *ApJ*, 898, 133
- Ma, C. J., Smail, I., Swinbank, A. M., et al. 2015, *ApJ*, 806, 257
- Mahajan, S., Mamon, G. A., & Raychaudhury, S. 2011, *MNRAS*, 416, 2882
- Maier, C., Hayashi, M., Ziegler, B. L., & Kodama, T. 2019a, *A&A*, 626, A14
- Maier, C., Ziegler, B. L., Haines, C. P., & Smith, G. P. 2019b, *A&A*, 621, A131
- Mantz, A., Allen, S. W., Ebeling, H., Rapetti, D., & Drlica-Wagner, A. 2010, *MNRAS*, 406, 1773
- Markevitch, M. 1998, *ApJ*, 504, 27
- Martí-Vidal, I., Vlemmings, W. H. T., Muller, S., & Casey, S. 2014, *A&A*, 563, A136
- McCracken, H. J., Milvang-Jensen, B., Dunlop, J., et al. 2012, *A&A*, 544, A156
- McMullin, J. P., Waters, B., Schiebel, D., Young, W., & Golap, K. 2007, in ASP Conf. Ser. 376, *Astronomical Data Analysis Software and Systems XVI*, ed. R. A. Shaw, F. Hill, & D. J. Bell (San Francisco, CA: ASP), 127
- Mohan, N., & Rafferty, D. 2015, *PyBDSF: Python Blob Detection and Source Finder*, *Astrophysics Source Code Library*, ascl:1502.007
- Molnár, D. C., Sargent, M. T., Leslie, S., et al. 2021, *MNRAS*, 504, 118
- Momcheva, I. G., Brammer, G. B., van Dokkum, P. G., et al. 2016, *ApJS*, 225, 27
- Mostoghiu, R., Arthur, J., Pearce, F. R., et al. 2021, *MNRAS*, 501, 5029
- Muzzin, A., Marchesini, D., Stefanon, M., et al. 2013a, *ApJS*, 206, 8
- Muzzin, A., Marchesini, D., Stefanon, M., et al. 2013b, *ApJ*, 777, 18
- Muzzin, A., Wilson, G., Yee, H. K. C., et al. 2012, *ApJ*, 746, 188
- Muzzin, A., van der Burg, R. F. J., McGee, S. L., et al. 2014, *ApJ*, 796, 65
- Nantais, J. B., Muzzin, A., van der Burg, R. F. J., et al. 2017, *MNRAS*, 465, L104
- Narayanan, D., Krumholz, M. R., Ostriker, E. C., & Hernquist, L. 2012, *MNRAS*, 421, 3127
- Noble, A. G., McDonald, M., Muzzin, A., et al. 2017, *ApJL*, 842, L21
- Noble, A. G., Muzzin, A., McDonald, M., et al. 2019, *ApJ*, 870, 56
- Noble, A. G., Webb, T. M. A., Yee, H. K. C., et al. 2016, *ApJ*, 816, 48
- Oman, K. A., Bahé, Y. M., Healy, J., et al. 2021, *MNRAS*, 501, 5073
- Oman, K. A., & Hudson, M. J. 2016, *MNRAS*, 463, 3083
- Oteo, I., Ivison, R. J., Dunne, L., et al. 2018, *ApJ*, 856, 72
- Patel, S. G., Holden, B. P., Kelson, D. D., Illingworth, G. D., & Franx, M. 2009, *ApJL*, 705, L67
- Peng, Y.-J., Lilly, S. J., Kovač, K., et al. 2010, *ApJ*, 721, 193
- Poole, G. B., Babul, A., McCarthy, I. G., et al. 2007, *MNRAS*, 380, 437
- Randall, S. W., Sarazin, C. L., & Ricker, P. M. 2002, *ApJ*, 577, 579
- Rhee, J., Smith, R., Choi, H., et al. 2017, *ApJ*, 843, 128
- Rhee, J., Smith, R., Choi, H., et al. 2020, *ApJS*, 247, 45
- Rosati, P., Borgani, S., & Norman, C. 2002, *ARA&A*, 40, 539
- Rudnick, G., Hodge, J., Walter, F., et al. 2017, *ApJ*, 849, 27
- Sanders, D. B., Salvato, M., Aussel, H., et al. 2007, *ApJS*, 172, 86
- Santos, J. S., Altieri, B., Tanaka, M., et al. 2014, *MNRAS*, 438, 2565
- Santos, J. S., Altieri, B., Valtchanov, I., et al. 2015, *MNRAS*, 447, L65
- Scoville, N., Arnouts, S., Aussel, H., et al. 2013, *ApJS*, 206, 3
- Shen, J., Man, A. W. S., Zabl, J., et al. 2021, *ApJ*, 917, 79
- Skelton, R. E., Whitaker, K. E., Momcheva, I. G., et al. 2014, *ApJS*, 214, 24
- Smolčić, V., Novak, M., Bondi, M., et al. 2017, *A&A*, 602, A1
- Speagle, J. S., Steinhardt, C. L., Capak, P. L., & Silverman, J. D. 2014, *ApJS*, 214, 15
- Stach, S. M., Swinbank, A. M., Smail, I., et al. 2017, *ApJ*, 849, 154
- Tacconi, L. J., Genzel, R., Saintonge, A., et al. 2018, *ApJ*, 853, 179
- Tacconi, L. J., Genzel, R., & Sternberg, A. 2020, *ARA&A*, 58, 157
- Tadaki, K.-i., Kodama, T., Hayashi, M., et al. 2019, *PASJ*, 71, 40
- Tadaki, K.-i., Kodama, T., Koyama, Y., et al. 2011, *PASJ*, 63, 437
- Taniguchi, Y., Scoville, N., Murayama, T., et al. 2007, *ApJS*, 172, 9
- Tran, K.-V. H., Papovich, C., Saintonge, A., et al. 2010, *ApJL*, 719, L126
- Umehata, H., Tamura, Y., Kohno, K., et al. 2017, *ApJ*, 835, 98
- Vikhlinin, A., Burenin, R. A., Ebeling, H., et al. 2009, *ApJ*, 692, 1033
- Virtanen, P., Gommers, R., Oliphant, T. E., et al. 2020, *NatMe*, 17, 261
- Vulcani, B., Poggianti, B. M., Finn, R. A., et al. 2010, *ApJL*, 710, L1
- Wang, T., Elbaz, D., Daddi, E., et al. 2018, *ApJL*, 867, L29
- Wang, T., Elbaz, D., Schreiber, C., et al. 2016, *ApJ*, 816, 84
- Waskom, M. L. 2021, *JOSS*, 6, 3021
- Wetzell, A. R., Tinker, J. L., Conroy, C., & van den Bosch, F. C. 2013, *MNRAS*, 432, 336
- Whitaker, K. E., Franx, M., Leja, J., et al. 2014, *ApJ*, 795, 104
- Whitaker, K. E., Labbé, I., van Dokkum, P. G., et al. 2011, *ApJ*, 735, 86
- Whitaker, K. E., Williams, C. C., Mowla, L., et al. 2021, *Natur*, 597, 485
- Wik, D. R., Sarazin, C. L., Ricker, P. M., & Randall, S. W. 2008, *ApJ*, 680, 17
- Williams, C. C., Labbe, I., Spilker, J., et al. 2019, *ApJ*, 884, 154
- Williams, C. C., Spilker, J. S., Whitaker, K. E., et al. 2021, *ApJ*, 908, 54
- Williams, R. J., Quadri, R. F., Franx, M., van Dokkum, P., & Labbé, I. 2009, *ApJ*, 691, 1879
- Yun, M. S., Reddy, N. A., & Condon, J. J. 2001, *ApJ*, 554, 803
- Zavala, J. A., Casey, C. M., Scoville, N., et al. 2019, *ApJ*, 887, 183
- Zeimann, G. R., Stanford, S. A., Brodwin, M., et al. 2013, *ApJ*, 779, 137
- Zinger, E., Dekel, A., Birnboim, Y., Kravtsov, A., & Nagai, D. 2016, *MNRAS*, 461, 412
- Zinger, E., Dekel, A., Kravtsov, A. V., & Nagai, D. 2018, *MNRAS*, 475, 3654